AIAA JOURNAL
Vol. 41, No. 2, February 2003

Hybrid Reynolds-Averaged Navier–Stokes/Large-Eddy Simulations of Supersonic Turbulent Mixing

Nicholas J. Georgiadis*
NASA John H. Glenn Research Center at Lewis Field, Cleveland, Ohio 44135
and
J. Iwan D. Alexander† and Eli Reshotko‡
Case Western Reserve University, Cleveland, Ohio 44106

A turbulent mixing layer formed from two supersonic streams initially separated by a splitter plate is investigated with a hybrid computational method using a Reynolds-averaged Navier–Stokes (RANS) approach for wall-bounded regions and a large-eddy simulation (LES) approach for the turbulent mixing region. Simulations of the mixing layer predict a vortex shedding originating from the splitter base and then a rapid transition to turbulence, which is in agreement with experimental observations. As a result, the potential of the hybrid method is demonstrated for flows in which a geometric feature, such as the blunt splitter plate considered here, provides the dominant unsteady feature leading to turbulence, without imposing additional inflow disturbances. Parametric studies of LES subgrid modeling settings, variations in the spanwise computational domain, and wall temperature settings in the RANS region were conducted. The subgrid model cases, using a baseline computational grid with small spanwise computational domain, overpredicted the mixing layer turbulence levels but only showed small variation in the mixing layer predictions with large changes in the model parameters. The cases examining wider spanwise domains enabled more turbulent energy to be released in the spanwise direction, which in turn reduced axial and vertical turbulence levels. Finally, prescribing the wall temperatures in the RANS regions instead of using the more traditional adiabatic wall boundary conditions further reduced turbulence levels and enabled reasonable agreement with experimental data.

Nomenclature

a	=	speed of sound
b	=	local mixing layer thickness between vertical positions where U is $U_{\text{top}} - 0.1\Delta U$ and U is $U_{\text{bottom}} + 0.1\Delta U$
C_h	=	Stanton number
C_I	=	Smagorinsky subgrid model (second) coefficient
C_P	=	specific heat at constant pressure
C_S	=	Smagorinsky subgrid model (first) coefficient
E_t	=	total energy
H	=	mixing duct height
k^{SGS}	=	effective subgrid thermal conductivity
P	=	static pressure
Pr^T	=	turbulent Prandtl number
q_j	=	heat flux
q_j^{SGS}	=	subgrid scale (SGS) heat flux
q_j^T	=	turbulent heat flux
q_w	=	wall heat flux
S	=	magnitude of the strain rate
S_{ij}	=	rate of strain tensor
T	=	static temperature
T_{aw}	=	adiabatic wall temperature
T_t	=	stagnation temperature
T_w	=	wall temperature
t	=	time
U	=	mean axial velocity
U_∞	=	freestream velocity
u, v, w	=	velocity components
u_i	=	velocity vector
u_{rms}	=	axial turbulent intensity
v_{rms}	=	vertical turbulent intensity
w_{rms}	=	spanwise turbulent intensity
x, y, z	=	Cartesian coordinates
x_i	=	position vector
Δ	=	filter width
ΔU	=	freestream velocity difference
$\Delta x, \Delta y, \Delta z$	=	Cartesian grid spacing
δ	=	boundary-layer thickness
δ_{ij}	=	Kronecker delta function
δ^*	=	displacement thickness
θ	=	momentum thickness
μ^{SGS}	=	SGS turbulent viscosity
π	=	SGS rate of strain parameter
ρ	=	density
τ_{ij}	=	viscous stress tensor
τ_{ij}^{SGS}	=	SGS stress
τ_{ij}^T	=	turbulent or Reynolds stress

Received 31 May 2001; presented as Paper 2001-2563 at the 15th Computational Fluid Dynamics Conference, Anaheim, CA, 11–14 June 2001; revision received 11 June 2002; accepted for publication 12 October 2002.

*Aerospace Engineer, Nozzle Branch. Senior Member AIAA.
†Professor, Department of Mechanical and Aerospace Engineering. Member AIAA.
‡Kent H. Smith Professor Emeritus, Department of Mechanical and Aerospace Engineering. Fellow AIAA.

Introduction

SIGNIFICANT research has been underway for several years in the development of advanced computational methods for simulation of turbulent flows in exhaust nozzles. The primary efforts of this research have concentrated on improving the capability of computational fluid dynamics (CFD) methods to calculate the compressible turbulent mixing layers that dominate the flows in exhaust systems of modern-day aircraft and hypersonic vehicles under development. To date, Reynolds-averaged Navier–Stokes (RANS) techniques have been used almost exclusively to calculate such flows. These RANS techniques require the use of turbulence models to replace all unsteady turbulent motion with a spatially varying eddy viscosity. Unfortunately, no turbulence model has been developed to date that is able to represent the turbulent motion accurately for

a broad range of flow conditions. Validation studies[1,2] have shown that the state-of-the-art turbulence models available in production-use RANS codes have major deficiencies in predicting turbulent mixing in nozzle and jet flows involving compressibility, high temperatures, and three dimensionality.

These limitations of RANS techniques have led to interest in techniques such as large-eddy simulation (LES) to improve the accuracy of calculating nozzle and jet flows dominated by turbulent mixing. In addition, LES offers the capability to produce a temporal history of the turbulent flow, which RANS methods inherently cannot provide. This feature has made LES an attractive technique for directly computing noise generation.

For realistic nozzle configurations in which upstream effects from wall bounded regions are important, applying an LES method to calculate the wide range of turbulent scales from very small scales in the wall bounded regions to large scales in the mixing region is not yet possible with current computers.[3] Nearly all LES simulations of jet and mixing layer flows performed to date have placed the inflow of the computational domain downstream of any wall bounded regions and have either ignored the upstream boundary-layer effects or used some approximation to initialize the turbulent mixing layer. The problem with using such artificially generated inflows is that the characteristics of the upstream boundary layers, including velocity, temperature, and turbulence profiles, are not accurately represented. This is a significant deficiency because the state of the incoming boundary layers have been shown to have substantial effects on the development of turbulent mixing layers in experiments conducted by Bradshaw,[4] Browand and Latigo,[5] and Hussain and Clark.[6]

To address the issues associated with modeling upstream wall boundary-layer effects, a hybrid method was recently developed by Georgiadis et al.[7] The hybrid method employs a RANS approach to provide the mean flow characteristics of the wall boundary layers entering the mixing region. The downstream mixing layer is then calculated using LES. The method developed here is intended for those nozzle and mixing layer problems in which a geometric feature, such as the base region of a nozzle or splitter plate separating the upstream flows, provides the dominant unsteady mechanism to drive the development of turbulence in the mixing layer. Although the upstream RANS approach does not provide any unsteady turbulence information to the mixing layer, the mean flow momentum and thermal boundary-layer effects are calculated and provided to the LES region. Figure 1 provides a schematic of a mixing layer configuration for which the current method is intended. This simple configuration is representative of more complex nozzle geometries in that two wall bounded regions provide isolated flows to a single region where compressible mixing is the primary flow characteristic.

Other hybrid RANS/LES methods have been recently developed and applied to a variety of flows. The most widely publicized hybrid technique to date is the detached-eddy simulation (DES) method.[3,8,9] In the DES method, wall bounded regions are calculated using RANS with the Spalart–Allmaras[10] one-equation turbulence model. A straightforward modification of the model for the turbulent length scale expression enables this RANS model to function as a subgrid model in LES regions. Constantinescu and Squires[11] have applied DES to turbulent flow over a sphere. Strelets[12] has used DES to investigate several flows for configurations with large-scale separation regions, including an airfoil at high angle of attack, a backward-facing step, and an aircraft landing gear truck. Batten et al.[13] proposed a hybrid model that employs a Reynolds-stress model to close the RANS and LES equations. Last, Arunajatesan et al.[14] and Arunajatesan and Sinha[15] have applied a hybrid RANS/LES method to cavity flowfields. Their approach employed a two-equation k–kl turbulence model to close the RANS equations and a one-equation model solving for the filtered subgrid kinetic energy to close the LES equations.

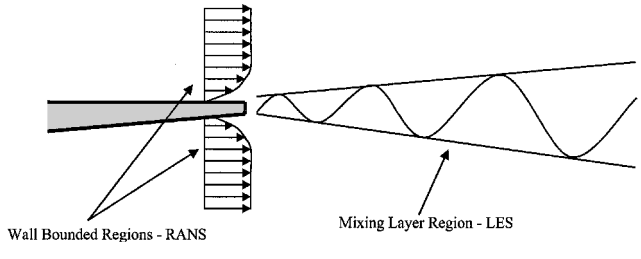

Fig. 1 Schematic of mixing layer demonstrating the hybrid RANS/LES approach.

The hybrid method used in this paper employs computationally inexpensive algebraic turbulence modeling for both the RANS and LES regions. A summary of the method is provided in the following section. Reference 7 provides details of the method development and preliminary calculations for the mixing layer configuration examined in the current work. Results indicated the capability of the RANS part of the hybrid method to accurately provide the mean flow characteristics of the wall boundary layers entering the mixing section. In the mixing region, the LES part of the method demonstrates an unsteady vortex shedding originating just downstream of the splitter plate separating the two wall bounded flows. This unsteady vortical structure rapidly transitions to a turbulent structure downstream in the mixing layer. Investigations of modeling issues associated with the hybrid method are the focus of this paper. Specifically, effects of subgrid modeling in the LES region, spanwise grid structure, and thermal boundary conditions applied to walls in the RANS region are examined.

Hybrid Numerical Method

To develop the hybrid method, both the RANS and LES equations were derived, starting from the compressible form of the Navier–Stokes equations. The details of this derivation are provided in Ref. 7 and will only be briefly described here. The RANS equations are derived using a density weighting in the time-averaging process. The resulting mass-weighted RANS equations for the continuity, momentum, and energy equations are

$$\frac{\partial \bar{\rho}}{\partial t} + \frac{\partial}{\partial x_i}(\bar{\rho}\hat{u}_i) = 0 \tag{1}$$

$$\frac{\partial}{\partial t}(\bar{\rho}\hat{u}_i) + \frac{\partial}{\partial x_j}(\bar{\rho}\hat{u}_i\hat{u}_j) + \frac{\partial \bar{P}}{\partial x_i} - \frac{\partial \bar{\tau}_{ij}}{\partial x_j} - \frac{\partial \tau_{ij}^T}{\partial x_j} = 0 \tag{2}$$

$$\frac{\partial}{\partial t}(\hat{E}_t) + \frac{\partial}{\partial x_j}(\hat{u}_j\hat{E}_t + \hat{u}_j\bar{P}) - \frac{\partial}{\partial x_j}\left(\hat{u}_i\bar{\tau}_{ij} + \hat{u}_i\tau_{ij}^T\right) + \frac{\partial}{\partial x_j}\left(\bar{q}_j + q_j^T\right) = 0 \tag{3}$$

To derive the LES equations, a spatial filtering procedure is applied to the time-dependent form of the Navier–Stokes equations to remove small-scale fluctuations that are too small to be resolved by the computational scheme. Similar to the process used for the RANS equations, a density weighting is used in the LES filtering process. The resulting LES expressions for conservation of mass, momentum, and energy are

$$\frac{\partial \bar{\rho}}{\partial t} + \frac{\partial}{\partial x_i}(\bar{\rho}\tilde{u}_i) = 0 \tag{4}$$

$$\frac{\partial}{\partial t}(\bar{\rho}\tilde{u}_i) + \frac{\partial}{\partial x_j}(\bar{\rho}\tilde{u}_i\tilde{u}_j) + \frac{\partial \bar{P}}{\partial x_i} - \frac{\partial \bar{\tau}_{ij}}{\partial x_j} - \frac{\partial \tau_{ij}^{\mathrm{SGS}}}{\partial x_j} = 0 \tag{5}$$

$$\frac{\partial}{\partial t}(\tilde{E}_t) + \frac{\partial}{\partial x_j}(\tilde{u}_j\tilde{E}_t + \tilde{u}_j\bar{P}) - \frac{\partial}{\partial x_j}\left(\tilde{u}_i\bar{\tau}_{ij} + \tilde{u}_i\tau_{ij}^{\mathrm{SGS}}\right) + \frac{\partial}{\partial x_j}\left(\bar{q}_j + q_j^{\mathrm{SGS}}\right) = 0 \tag{6}$$

In Eqs. (1–3), the terms denoted with a carat are mass-weighted, time-averaged quantities. In this case, τ_{ij}^T and q_j^T are replaced with a turbulence model. In Eqs. (4–6), the terms denoted with a tilde are mass-weighted, spatially filtered quantities, and τ_{ij}^{SGS} and q_j^{SGS} are also replaced with a model. The modeled SGS stresses, however, are only those that are too small to be resolved by the computational scheme and grid, whereas the entire spectrum of turbulent stresses is replaced with a model in the RANS equations. Because of the similar form of the RANS and LES equations, both equation

sets are solved with a single computational method. In this work, the Gottlieb–Turkel scheme[16] was used. This predictor–corrector scheme is second-order accurate in time and fourth-order accurate in space. In addition, the equations are transformed to generalized coordinates and solved with a set of metric terms that are consistent with the Gottlieb–Turkel scheme.

Closure for the RANS equations is obtained using the Cebeci–Smith[17,18] algebraic turbulence model in conjunction with the wall-function approach of Ota and Goldberg.[19] The use of wall functions relaxes the near-wall spacing in the RANS region to enable a continuous computational grid from the RANS regions to the LES region. This RANS turbulence modeling procedure is described more extensively in Ref. 7. Because variations of the SGS model parameters are considered in this paper, details of the model are provided next. The LES equations are closed using the Smagorinsky SGS model.[20] The form of the model is similar to the Cebeci–Smith[18] model used for the RANS equations in that a gradient-diffusion mixing-length approach is used.

The Smagorinsky[20] expression for the SGS stress is

$$\tau_{ij}^{\mathrm{SGS}} = 2\bar{\rho}(C_S\Delta)^2 S\left(\tilde{S}_{ij} - \tfrac{1}{3}\tilde{S}_{kk}\delta_{ij}\right) - \tfrac{2}{3}C_I\Delta^2\bar{\rho}S^2\delta_{ij} \qquad (7)$$

where S is obtained from

$$S = \sqrt{2\tilde{S}_{ij}\tilde{S}_{ij}} \qquad (8)$$

The parameter Δ is the length scale used in the spatial filtering of the equations and, as a result, is used as the characteristic length scale of the subgrid turbulence. For this method, Δ is taken to be the grid spacing. In a three-dimensional computational grid with unequal spacing in each direction, this subgrid length scale is frequently defined as

$$\Delta = (\Delta x\Delta y\Delta z)^{\frac{1}{3}} \qquad (9)$$

For computational grids with substantially different spacing in the three directions, an alternative form[21] is

$$\Delta = \{[(\Delta x)^2 + (\Delta y)^2 + (\Delta z)^2]/3\}^{\frac{1}{2}} \qquad (10)$$

For the same computational grid, the modified length scale expression results in larger values of the subgrid model eddy viscosity compared to the standard length scale expression. Both expressions for the length scale are examined in this work. The SGS eddy viscosity is analogous to the eddy viscosity used in RANS turbulence models and is written as

$$\mu^{\mathrm{SGS}} = \bar{\rho}(C_S\Delta)^2 S \qquad (11)$$

The constants C_S and C_I have been found to be dependent on the flow under investigation. Rogallo and Moin[22] suggest a range for C_S of $0.10 \le C_S \le 0.24$. These limits on C_S were investigated for the mixing layer in this work. The constant C_I is usually equal to 0.01, but several authors, including Ragab and Sheen[21] and Choi et al.[23] mention that the contribution of the term involving C_I may not be important and may be neglected. The latter approach is taken in this work. The SGS heat flux is modeled analogously to that done for the turbulent heat flux of the RANS equations:

$$q_j^{\mathrm{SGS}} = -k^{\mathrm{SGS}}\frac{\partial\tilde{T}}{\partial x_j} \qquad (12)$$

where k^{SGS} is related to μ^{SGS} through the turbulent Prandtl number. As in the RANS regions, the turbulent Prandtl number is assumed to be constant in the LES regions and equal to 0.9. The SGS heat flux becomes

$$q_j^{\mathrm{SGS}} = -\frac{C_P}{Pr^T}\bar{\rho}(C_S\Delta)^2 S\frac{\partial\tilde{T}}{\partial x_j} \qquad (13)$$

Solution Procedure

The quantities in the RANS equations (1–3) represent time-averaged quantities and are fundamentally different from the spatially filtered quantities in the LES equations (4–6). However, the similar structural form of these two equation sets enables a simulation to be calculated continuously from the RANS regions through the LES region. This is accomplished through the turbulence modeling by using the Cebeci–Smith[18] RANS closure upstream of the vertical plane passing through the splitter plate trailing edge and using the Smagorinsky[20] LES closure downstream of this plane. In addition, for the mixing layer simulations considered here, a continuous three-dimensional grid is used from the RANS regions to the LES region. The flows in the RANS regions essentially reach a steady state that also does not vary spatially in the spanwise direction as a calculation progresses. However, three-dimensional calculations are continued everywhere to preserve the coupling of the RANS and LES regions.

Whereas the mean flow properties of the boundary layers are provided to the LES region with the developing mixing layer, no disturbances are specified to the beginning of the mixing layer, as is frequently required to establish turbulence in LES simulations of mixing layers. However, as will be demonstrated in the computational results section, the modeling of the splitter plate trailing edge enables an unsteady vortex shedding to be simulated at the beginning of the mixing layer. It is this vortex shedding that provides the dominant instability to drive a rapid transition of the mixing layer to a turbulent state.

Experimental Configuration

The hybrid RANS/LES method was applied to one of the benchmark mixing layer experiments of Goebel–Dutton[24,25] referred to as case 2, in which two isolated supersonic streams, separated by a splitter plate, provide the flows to a mixing section. The operating conditions of the two streams in case 2 are provided in Table 1. The convective Mach number calculated from the flow conditions is 0.46. The higher-speed primary stream occurred over the top surface of the splitter plate. The top stream enters the mixing section axially, whereas the bottom stream enters the mixing section at an angle of 2.5 deg. The splitter plate thickness has a base height of 0.5 mm at the trailing edge. Upstream of the straight sections for the two isolated flows, contoured nozzle blocks provided the supersonic flows.

The mixing section height was 48 mm, and the length of the mixing section available for flowfield measurements was 500 mm. The width of the mixing section was 96 mm, and, as a result, the mean flow development could be considered two-dimensional. The lower and upper walls of the mixing section could be adjusted to account for boundary-layer growth along these two surfaces and, as a result, effectively remove any streamwise pressure gradient.

Single-component laser Doppler velocimetry (LDV) measurements were used to calculate boundary-layer, displacement, and momentum thicknesses of the two streams as they entered the mixing section. These quantities are provided in Table 1. Such documentation of the incoming boundary-layer characteristics makes the Goebel–Dutton experiments one of the more thoroughly documented benchmark data sets available for compressible mixing layers. In the mixing region, a two-component LDV system was used to measure the axial and vertical velocities. In addition, a schlieren system with a 20-ns pulse duration was used to obtain nearly instantaneous photographs of the mixing layer.

Table 1 Flow conditions for case 2 of the Goebel–Dutton experiments

Parameter	Top flow	Bottom flow
Mach no.	1.91	1.36
U, m/s	700	399
T_t, K	578	295
T, K	334	215
a, m/s	366	293
P, kPa	49	49
ρ, kg/m^3	0.51	0.79
δ, mm	2.9	2.5
δ^*, mm	0.90	0.44
θ, mm	0.29	0.21

Computational Results

SGS Model Parameter Variations

Whereas the mean flow is two-dimensional in nature, three-dimensional calculations are necessary to compute the large-scale turbulence directly. In the initial calculations obtained in Ref. 7 for this mixing layer configuration, computational grids having 200, 400, and 800 axial points in the LES region were examined. The grids having 400 and 800 axial points both were able to capture the unsteady vortical structure in the initial part of the mixing layer that rapidly transitioned to a turbulent structure. These two grids also predicted nearly identical mixing layer structures farther downstream. The grid containing 200 axial points did not provide sufficient resolution to enable the unsteady vortex shedding, nor any realistic turbulent structure farther downstream. As a result, the grid containing 400 points in the axial direction, 197 points in the vertical direction, and 11 points in the spanwise direction was used as the baseline for the calculations discussed in this section. The axial domain extended 300 mm from the trailing edge of the splitter plate. The grid points were clustered to the splitter plate trailing edge such that $\Delta x_1 = 0.10$ mm. In the vertical direction, the grid was packed to the two sides of the splitter plate with initial spacing set to $\Delta y = 0.05$ mm $= \frac{1}{2}\Delta x_1$, or one-tenth of the splitter plate thickness at the trailing edge. In addition, 10 grid points were equally spaced vertically across the splitter plate trailing edge to enable resolution of the unsteady vortex street that initiates the mixing layer development. The grid spacing in the spanwise (z) direction was uniform and set equal to the axial spacing at the splitter trailing edge, or $\Delta z = \Delta x_1 = 0.10$ mm. A periodic boundary condition for all flow quantities was used in this direction. The very small number of grid points used in the z direction and the small physical space that is represented limited the size and wave numbers of the turbulent structures that could be captured by the computation in the spanwise direction. However, this compromise was necessary to enable enough points to be used in the other two computational directions for providing sufficient resolution to capture the important unsteady vortex structure. Furthermore, the grid stretching in the axial direction had to be kept to a minimum (less than 1%) to prevent contamination of the unsteady flow structure in the critical region just downstream of the splitter base.

Upstream of the LES region, the two wall bounded streams were calculated using the RANS approach with grid domains containing 61 axial points and 94 vertical points. The Δx and Δy spacings exactly matched those of the LES region at the RANS/LES interface. The wall boundary conditions were set as adiabatic no-slip surfaces. Reference 7 discussed in detail the procedure used to generate boundary-layer profiles with displacement and momentum thicknesses that matched those measured in the experiment just upstream of the beginning of the mixing section.

Considerable research into SGS modeling has resulted in a variety of models that are currently used in LES. Recently, Spalart[3] and Fureby and Grinstein[26] have suggested the possibility of performing an LES without an SGS model, provided that the simulation resolves the dominant energy containing turbulent scales. In this section, the effects of variations in the relatively simple Smagorinsky[20] SGS model are investigated. Three calculations were completed in which the Smagorinsky SGS model parameters (the constant C_S and the SGS length scale) were varied. The first case used the standard length scale expression given by Eq. (9) and $C_S = 0.10$. The second case also used the standard length scale expression and $C_S = 0.24$. The third case used the modified length scale expression given by Eq. (10) and $C_S = 0.24$. With the limited spanwise grid and simple SGS model used here, the objective is not to conduct a comprehensive study of SGS model variations, but only to determine gross effects of the SGS model constant C_S and the length scale expression on the calculated mixing layer evolution. By the examination of the two typical bounds on C_S, and the two different length scale expressions (9) and (10), large variations in the subgrid eddy viscosity could be examined. Attempts at running the procedure with no SGS model resulted in solution divergence.

Figure 2 shows a comparison of density in the first one-half of the axial domain obtained with the third case to a two-dimensional simulation obtained with an x–y plane extracted from the three-dimensional grid. Both solutions exhibit a periodic vortex shedding that originates from the splitter plate trailing edge. However, for the three-dimensional case, there is a rapid transition to turbulence. The vortex shedding and transition behavior was very similar for all of the three-dimensional cases discussed in this and the other sections of this paper, with a shedding frequency corresponding to a Strouhal number of 0.13. Although the vortex strength and transition behavior of the two-dimensional case was very different from the three-dimensional solutions, the shedding frequency was the same.

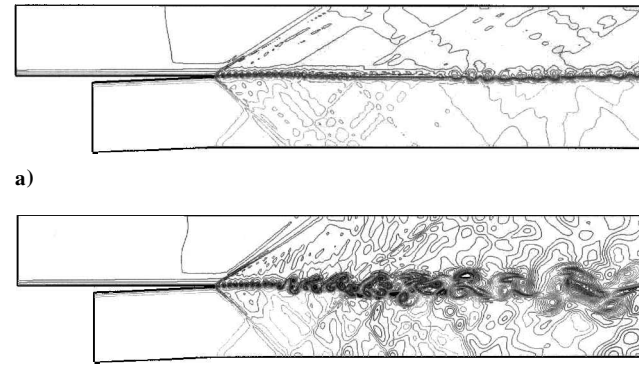

Fig. 2 Comparison of instantaneous density contours in mixing section: a) two-dimensional case with no subgrid model and b) three-dimensional case with the standard turbulent length scale and $C_S = 0.24$

Density contours are useful for visualizing the flow in the mixing region and provide a computational analogy to the schlieren photographs that are used in experiments. Although the strongest gradients of the density are observed in the developing shear layer, gradients are also observed in the regions above and below the mixing layer. These are the result of Mach waves generated by the unsteady mixing layer and their interaction with the two walls of the confined mixing section. Such waves were also evident in the schlieren photographs of the Goebel–Dutton experiments. In Ref. 27, the effects of the wave reflections from the walls on the mixing layer development were investigated. Calculations were obtained in which extra grid points were added vertically to move each wall very far from the mixing layer, so that the effective mixing section height became 900 mm. This extreme spacing resulted in all waves originating from the splitter plate trailing edge to pass out of the outflow boundary without the opportunity to reflect back onto the mixing layer. The resulting mixing layer development was very similar to that of the baseline, and it was concluded that the reflection of the waves from the mixing section walls does not affect the mixing layer behavior.

Details of the transition behavior of the initially organized vortex street to a turbulent flow are provided by the 12 photographs of the density shown in Fig. 3, again for the third three-dimensional case. The region shown in these photographs is a close-up of the flow very near the splitter plate trailing edge. Each successive photograph represents a march forward in time of 3.7×10^{-6} s, which corresponds to 250 time steps obtained with the Gottlieb–Turkel[16] predictor–corrector scheme. This time interval was chosen such that in every other photograph, a new vortex is shed from the trailing edge of the splitter. The initial organized vortex pattern is followed by a vortex pairing and transition to turbulence, which is very similar to the flow development observed in the experiments. The vortex shedding, transition, and initial turbulent structures were very similar for all of the three-dimensional cases investigated in this work. In addition, the number of organized vortices before breakdown to turbulence may change for the time progression shown. However, all of the calculations examined in this work oscillated between having 5 and 10 organized vortices before transition occurred.

The mean axial velocity profiles obtained from the three calculations in which the subgrid model parameters were varied, but all using the baseline three-dimensional grid, are compared to the Goebel–Dutton data in Fig. 4. All of the solutions exhibit a larger wake at $x = 50$ mm than that of the experiment. Farther downstream, all of the solutions appear to mix more rapidly than indicated by the experimental data. Comparisons of the axial and vertical turbulence

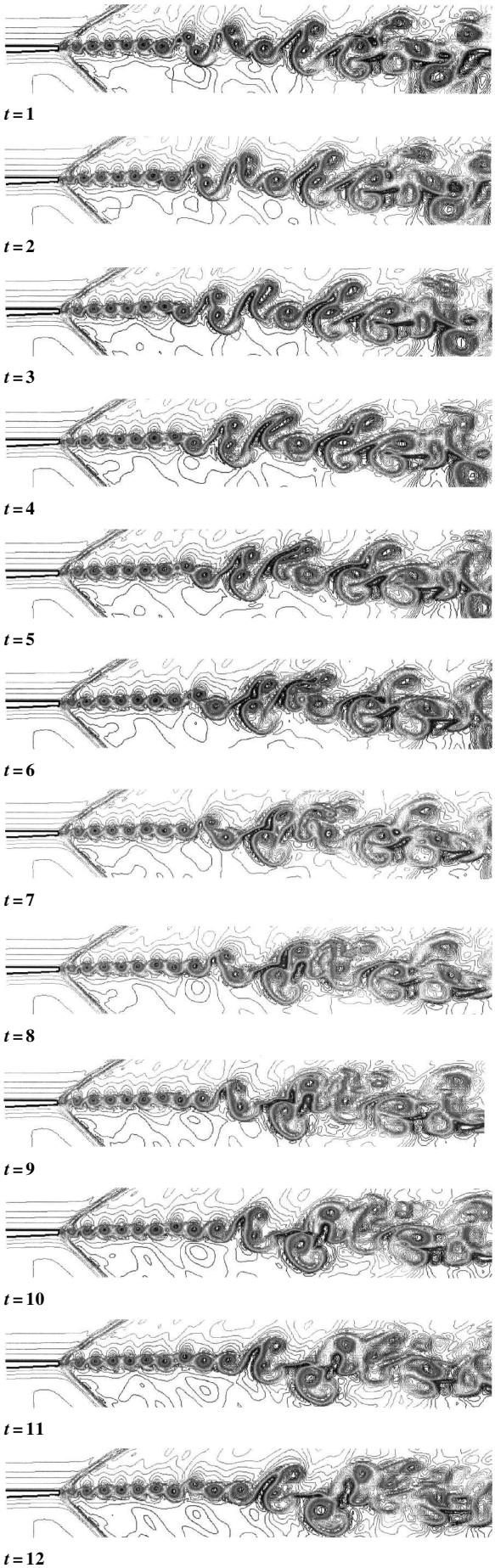

Fig. 3 Time series of instantaneous density contours for the three-dimensional hybrid calculation using the modified length scale expression and $C_S = 0.24$.

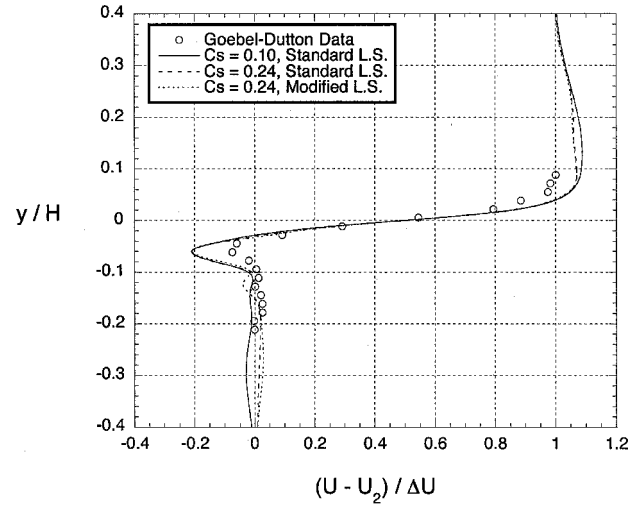

a) $X = 50$ mm

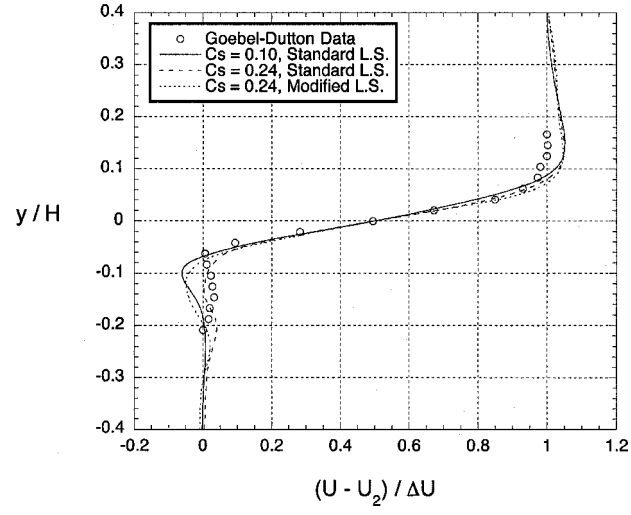

b) $X = 100$ mm

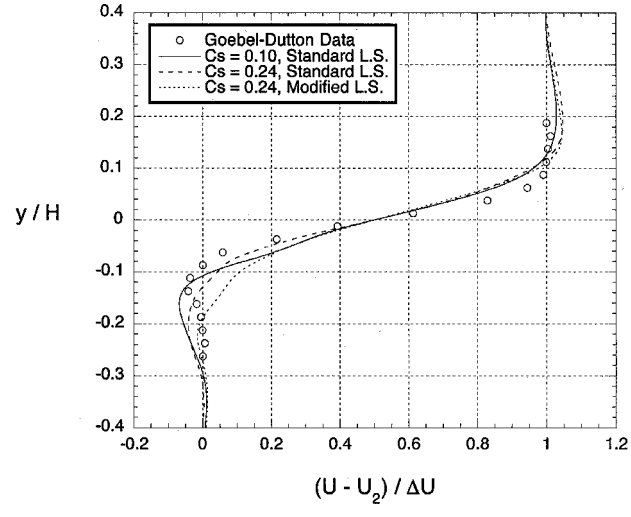

c) $X = 150$ mm

Fig. 4 Time-averaged axial velocity profiles for the cases investigating SGS effects.

intensities are made in Figs. 5 and 6, respectively. The u_{rms} and v_{rms} quantities are obtained from the long time averages of the resolved velocity components and do not include any SGS contribution. Figure 5 shows that the calculations generally overpredict u_{rms}, which corresponds to the wider axial velocity profiles in Fig. 4. At $x = 50$ mm, a double peak in the calculated intensities is evident for all of the calculations. Farther downstream, the solution obtained with $C_S = 0.24$ and the modified length scale demonstrates generally

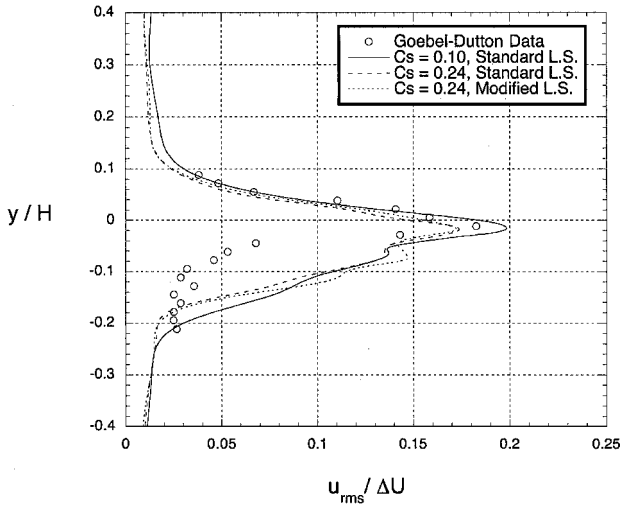

a) $X = 50$ mm

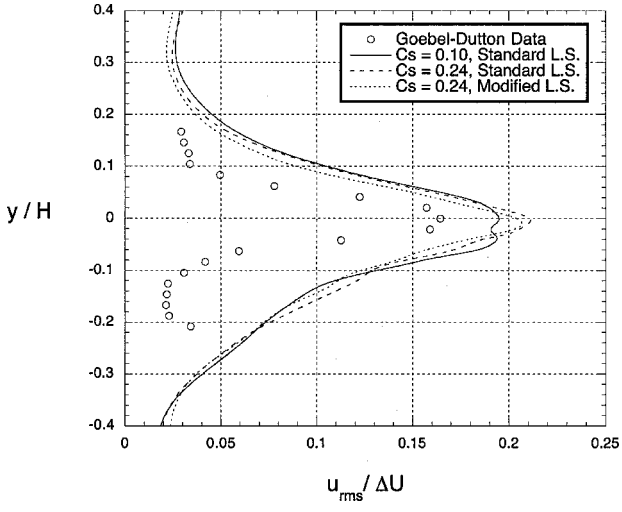

b) $X = 100$ mm

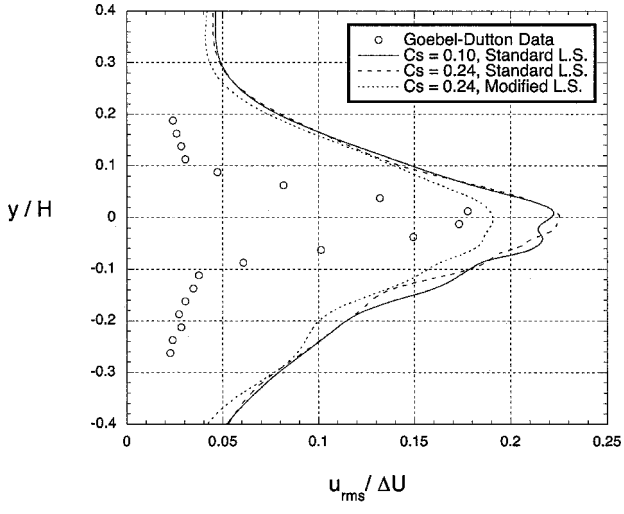

c) $X = 150$ mm

Fig. 5 Profiles of u_{rms} for the cases investigating SGS effects.

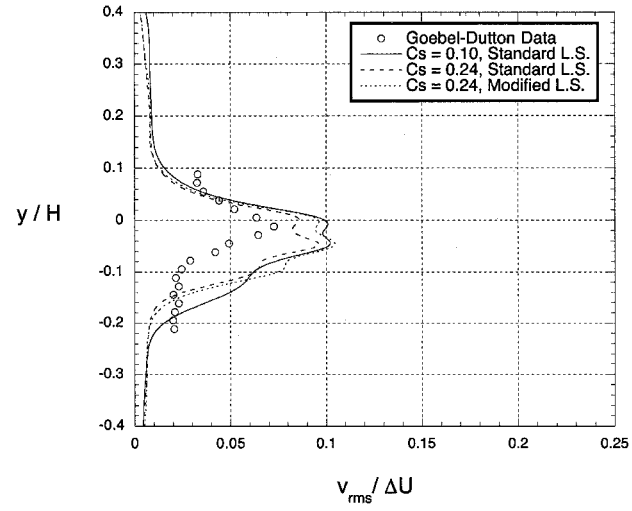

a) $X = 50$ mm

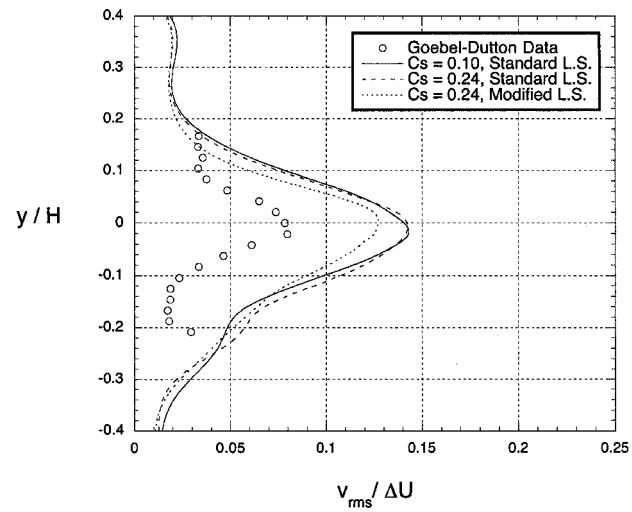

b) $X = 100$ mm

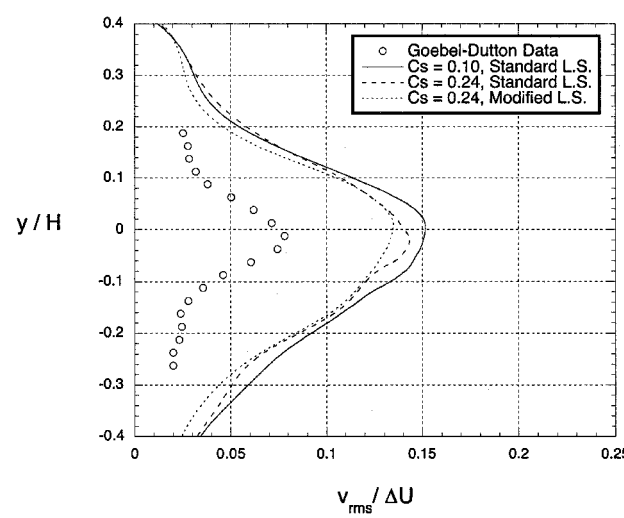

c) $X = 150$ mm

Fig. 6 Profiles of v_{rms} for the cases investigating SGS effects.

lower levels of u_{rms} than the other solutions. From Eq. (11), this combination produces the largest SGS viscosities. Although increasing the Smagorinsky constant C_S also tends to result in more damping, the effect of changing C_S from 0.10 to 0.24 does not seem to have as large an effect as the SGS length expression.

The computed profiles of v_{rms} shown in Fig. 6 are also overpredicted relative to the data, with the lowest levels of v_{rms} predicted with the modified length scale and $C_S = 0.24$. The turbulent fluctuations in the z direction cannot be properly resolved due to the grid width and forced periodicity in this direction. This inability to capture large-scale fluctuations in the spanwise direction is hypothesized to be a primary contributor to the overpredictions of u_{rms} and v_{rms}; however, note again that the objective of these SGS studies was only to determine gross effects of model parameter variations on the mixing layer development. Hybrid calculations in which the spanwise computational grid was expanded are discussed in the next section.

Spanwise Grid Variations

As mentioned in the preceding section, the grid resolution in the z direction and the small physical domain in this direction prohibited the formation of any large-scale turbulence in the spanwise (z) direction for all of the cases examined. As a first modification to the spanwise grid structure, the spacing was doubled to $\Delta z = 0.20$ mm. The number of points was kept at 11. A computation was performed with this modified computational grid and using the modified SGS length scale expression with $C_S = 0.24$. Results for this case were nearly identical to those from the case using the original grid and same SGS model settings.

The next two grids that were examined used the $\Delta z = 0.20$ mm spacing and increased the number of spanwise points to 21 and 31, such that the overall spanwise domain widths were doubled and tripled, respectively. As a result, not only were more spanwise grid points used, but the spanwise physical domain was increased so that more realistic flow development could be simulated in this direction. Table 2 provides a summary of the spanwise grid structure variations. To accommodate the limited memory requirements of the computer used (a Cray C90 vector machine), the axial domain was shortened to 150 mm by truncating the last 80 axial points of the original grid. The widths of the two new grids, 4 and 6 mm, respectively, were on the order of the mixing layer thickness measured in the experiment, 5 mm, at the axial position corresponding to $x = 150$ mm. Because of the supersonic nature of the mixed flow, moving the outflow toward the splitter would not affect the flowfield upstream. This was verified in preliminary calculations with the two new grids.

Computations were performed with these two modified computational grids, again using the modified SGS length scale expression and $C_S = 0.24$. Figure 7 shows instantaneous constant density surfaces in the mixing layer and illustrates that as the spanwise width is increased, more three-dimensional growth is enabled. Only the last one-half of the RANS domains and the first one-half of the LES domain are shown in Fig. 7 to show the detail near the transition and early turbulent region. Figure 8 shows a comparison of mean axial velocity profiles for the cases investigating spanwise grid variations. Comparisons of the two turbulence intensities measured in the experiment are provided in Figs. 9 and 10. Although no experimental measurements were made in the spanwise direction, the spanwise turbulence intensities obtained from the calculations are presented in Fig. 11. At $x = 50$ and 100 mm, the calculated velocity profiles in the high shear mixing region exhibit similar behavior. However, farther downstream at $x = 150$ mm, the two solutions obtained with 4- and 6-mm widths predict less mixing layer growth and are in closer agreement with the experimental measurements. The axial turbulence intensities obtained from the two calculations with 4- and 6-mm widths, respectively, generally indicate less overprediction of the peak intensities relative to the experimental data. The vertical turbulence intensities are still overpredicted relative to the experimental data, but the peak intensities obtained with 4- and 6-mm width domains are closer to the data than the original calculation with a 2-mm width.

The spanwise turbulence intensities shown in Fig. 11 indicate substantially different flow development in the z direction when the computational domain is varied in this direction. The calculation with a 2-mm width indicates almost no turbulent fluctuations. However, increasing the width of the physical domain using the other two grids does allow for spanwise-varying turbulence to grow. In addition, streamwise braid vortices are evident for the 4- and 6-mm width cases, but not for the 2-mm width case. The discrepancies between the 4- and 6-mm spanwise width cases is small at $x = 50$ mm, but becomes larger farther downstream. At $x = 50$ mm, the size of the turbulent eddies are sufficiently small to be captured relatively well with the grids having 4- and 6-mm widths.

Table 2 Spanwise grid structure variations

Spanwise points	Δz, mm	Total width, mm
11 (SGS studies)	0.10	1.00
11 (current)	0.20	2.00
21 (current)	0.20	4.00
31 (current)	0.20	6.00

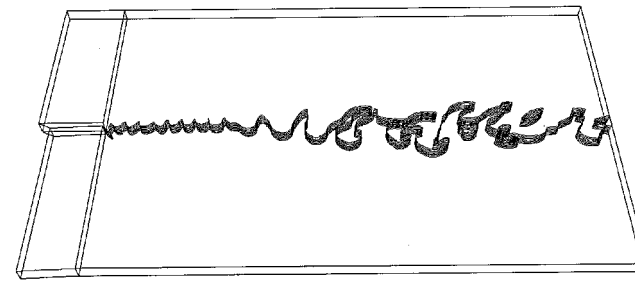

a) Spanwise width = 2 mm

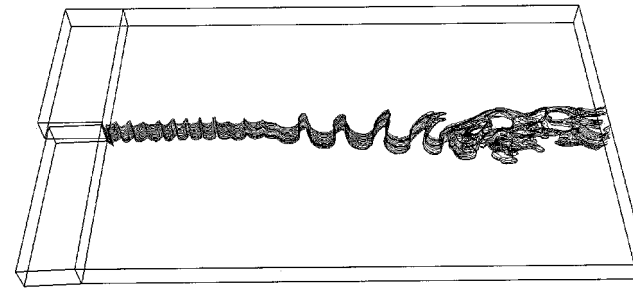

b) Spanwise width = 4 mm

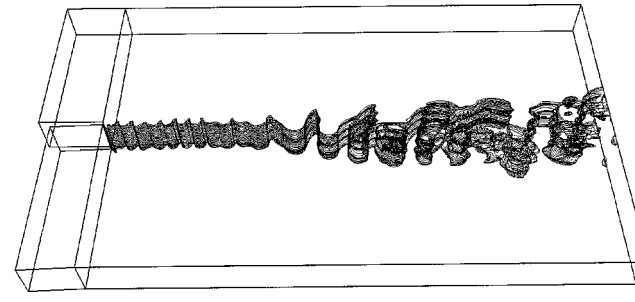

c) Spanwise width = 6 mm

Fig. 7 Instantaneous constant density surfaces in mixing layer, $\rho = 0.5$ ($\rho_{top} + \rho_{bottom}$).

Farther downstream, as the size of the eddies approaches and eventually exceeds the spanwise width of the computational grid, the widest (6-mm) spanwise case is better able to capture the larger eddies than the 4-mm width case. In addition, the peak intensities also drop from $x = 100$ to 150 mm for each of these two cases. This indicates that as the magnitude of the largest three-dimensional eddies grows with axial position, the ability to simulate the spanwise growth is reduced.

The calculations discussed in this section only begin to address the effects of the spanwise domain. However, the significant effects of widening the domain to enable some turbulent structures to be captured may be observed from these calculations. In particular, the reduction in the axial and vertical turbulence intensities compared to the calculations performed with the 2-mm width grid is enabled by allowing some of the turbulent energy production to be released in the spanwise direction for the two cases with 4- and 6-mm widths.

The initial computational grid was sufficient to enable formation of the initial disturbances critical to the transition of the organized vortical structure to the turbulent mixing layer. These disturbances were sufficiently small such that they were not affected by the limitations of the spanwise domain. Examination of all of the calculations indicated that the initial disturbance formation and magnitude, as well as the resulting transition behavior, was virtually the same for all of the grids. This is also shown by the constant density surfaces shown in Fig. 7. Although the mean flow is two-dimensional, the turbulent structures in the mixing layer are clearly three-dimensional in nature. Increasing the spanwise domain further, to the eventual limit of modeling the actual width of the experiment, would be desirable but would require currently prohibitive computational resources.

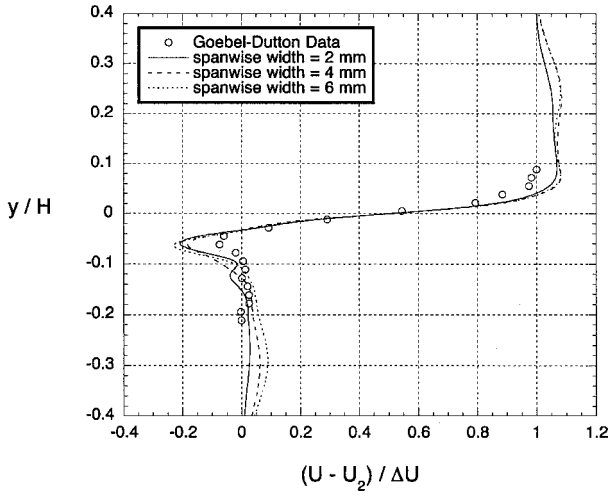

a) $X = 50$ mm

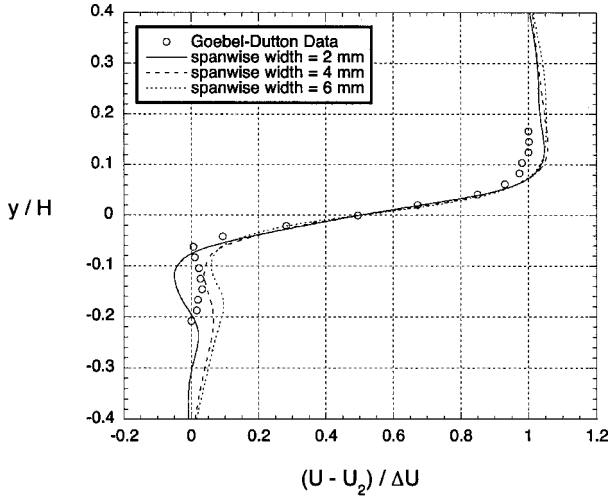

b) $X = 100$ mm

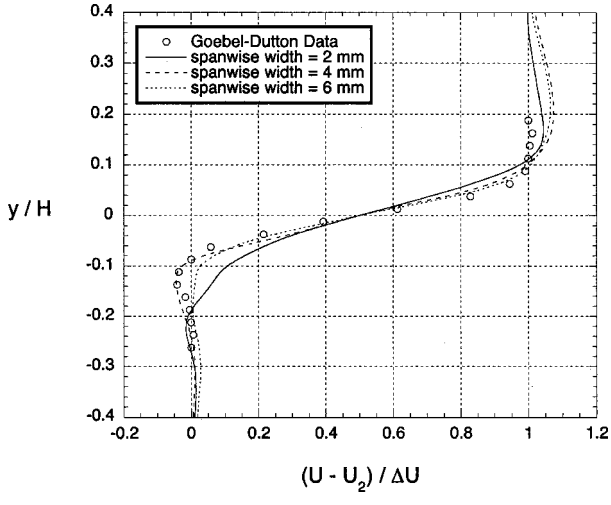

c) $X = 150$ mm

Fig. 8 Time-averaged axial velocity profiles for the cases investigating spanwise grid variations.

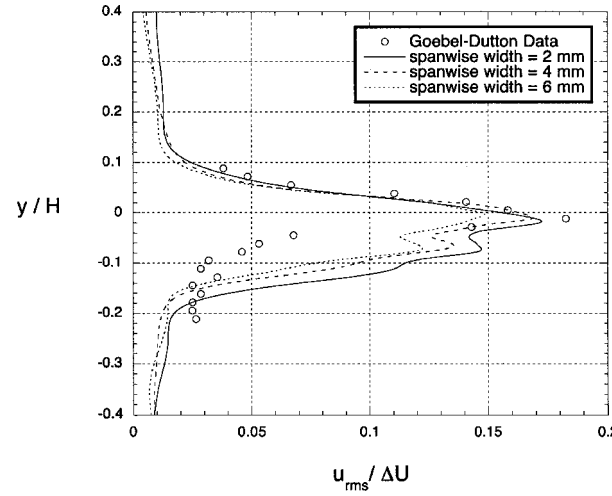

a) $X = 50$ mm

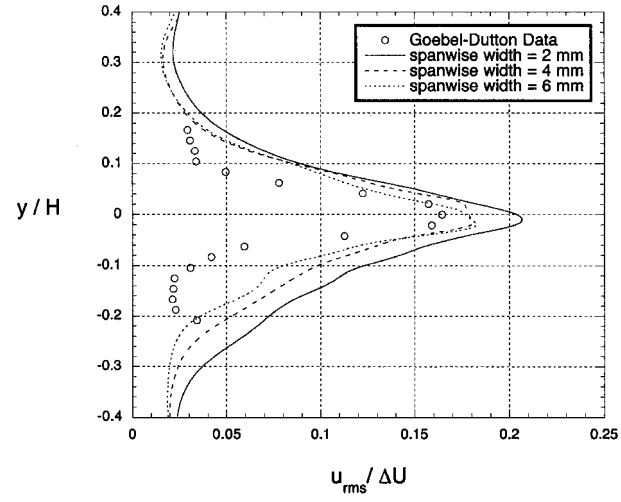

b) $X = 100$ mm

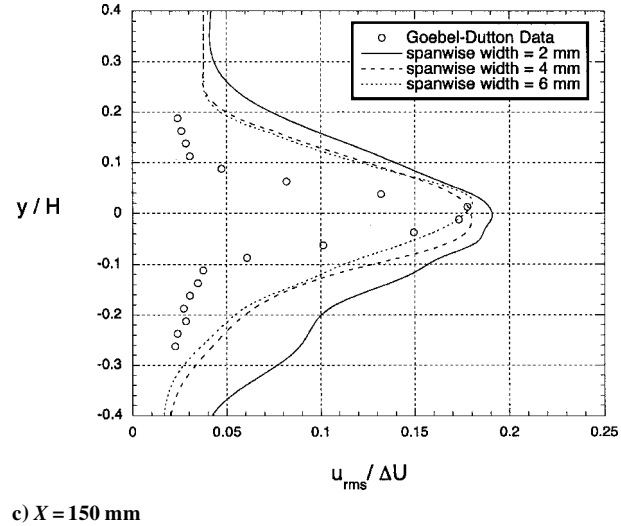

c) $X = 150$ mm

Fig. 9 Profiles of u_{rms} for the cases investigating spanwise grid variations.

RANS Thermal Boundary Condition Variations

In this section, effects of the boundary conditions used for the no-slip surfaces in the RANS regions are investigated. In all of the cases discussed thus far, adiabatic surfaces were assumed, as is most frequently the case for RANS simulations of wall boundary layers. However, with only a very thin stainless-steel splitter plate separating the heated and unheated streams, the two surfaces of the splitter plate were apt to be at substantially different temperatures than the adiabatic wall temperatures of the two streams.

A simple heat transfer analysis of the splitter plate was used to obtain wall temperatures for an additional case investigating wall thermal boundary condition effects. This analysis consisted of equating the heat transfer from each stream to that conducted vertically through the stainless-steel plate, or

$$q_w = C_h \rho_\infty U_\infty C_p (T_w - T_{aw}) = -\left(k \frac{\partial T}{\partial y}\right)_w \qquad (14)$$

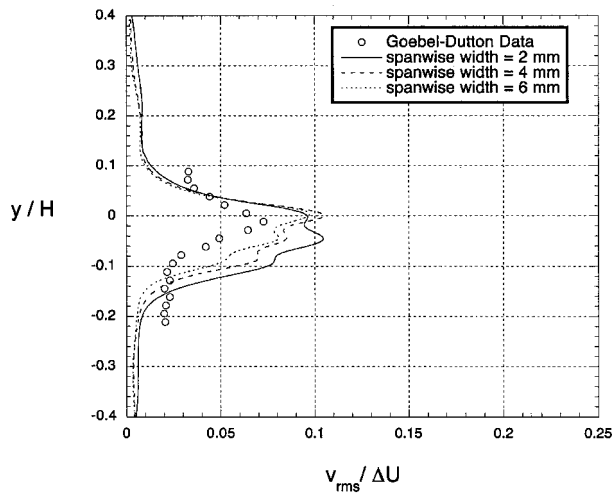

a) $X = 50$ mm

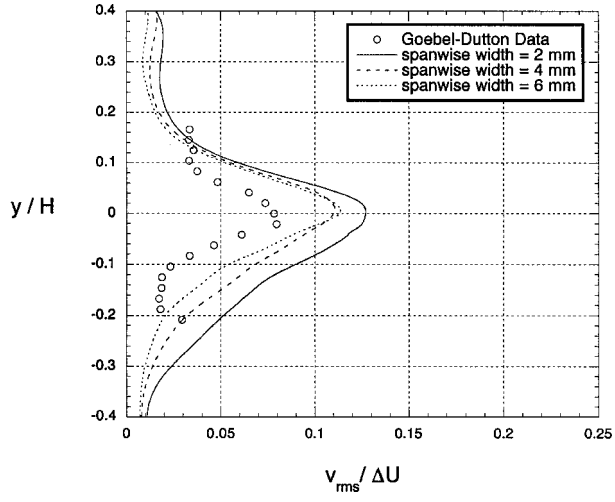

b) $X = 100$ mm

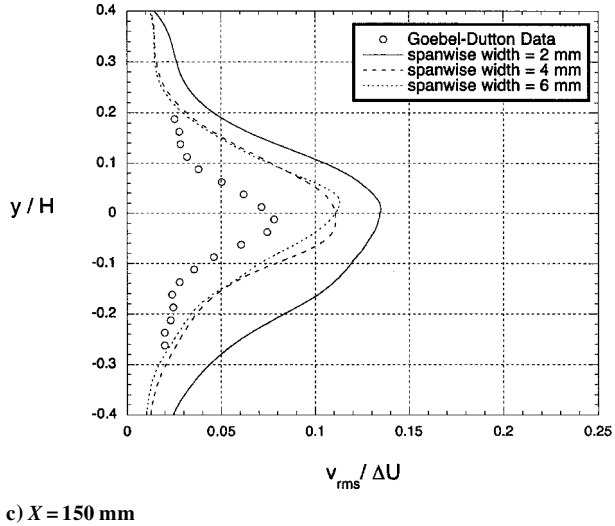

c) $X = 150$ mm

Fig. 10 Profiles of v_{rms} for the cases investigating spanwise grid variations.

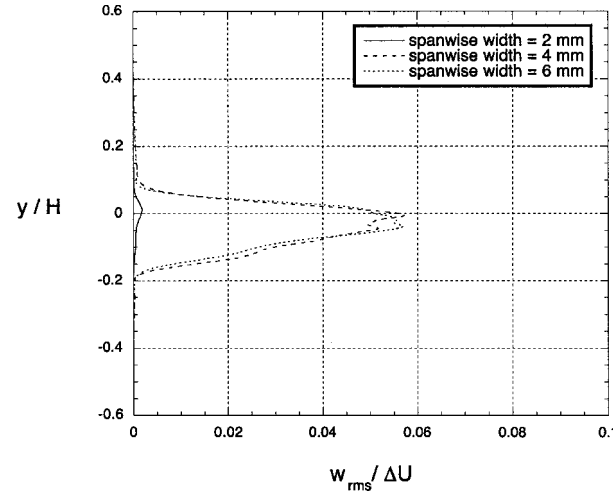

a) $X = 50$ mm

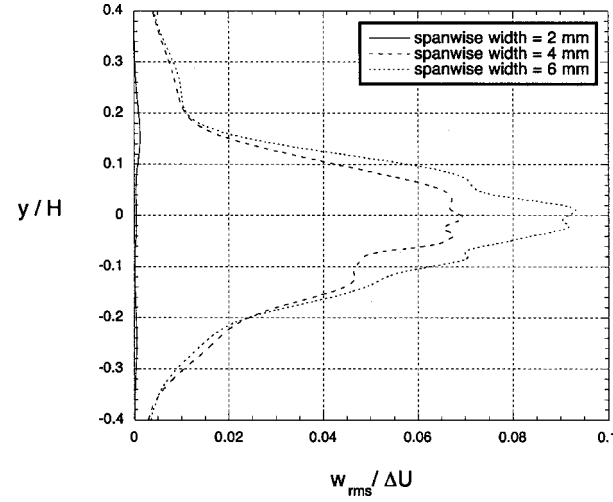

b) $X = 100$ mm

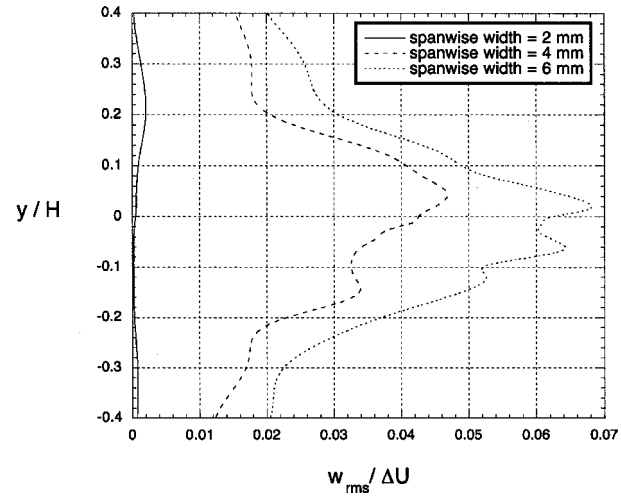

c) $X = 150$ mm

Fig. 11 Profiles of w_{rms} for the cases investigating spanwise grid variations.

For 304 stainless steel, the thermal conductivity is 14.4 W/m · K. An expression for the Stanton number is employed, using the Reynolds analogy such as that from White[28]

$$C_h = 0.62 C_f \tag{15}$$

Two expressions, one for the top flow and the other for the bottom flow, could be written using Eq. (14) with skin-friction coefficients obtained from earlier calculations in the RANS regions. Given a linear variation of temperature vertically through the plate at any axial station, these two expressions are simultaneously solved to obtain the two wall temperatures as a linear function of the splitter plate thickness. It was found that the maximum difference in (axially varying) temperatures from one surface of the plate to the other was substantially less than the difference of the two adiabatic wall temperatures, 552 K for the top flow and 286 K for the bottom flow. At the trailing edge of the plate, the calculated temperature difference was less than 3 K. In addition, at every axial station, the average of the two surface temperatures was equal to 419 K.

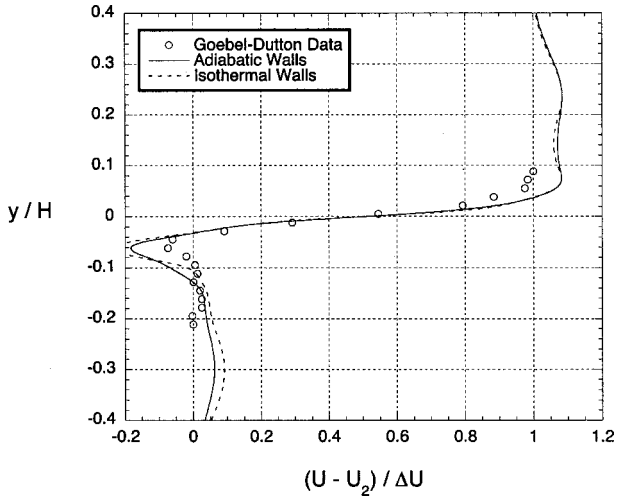

a) $X = 50$ mm

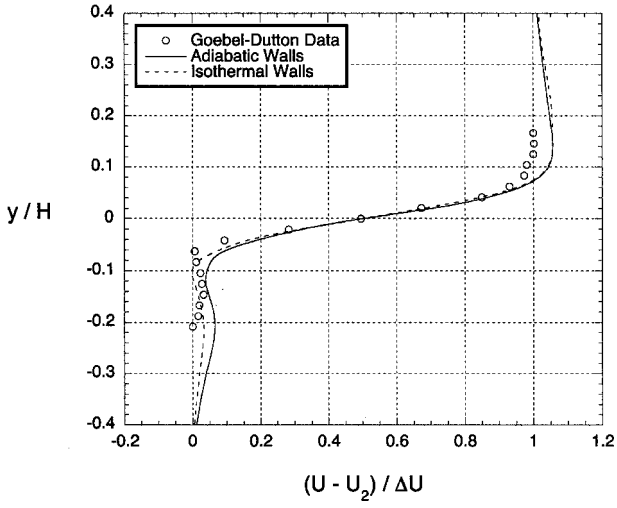

b) $X = 100$ mm

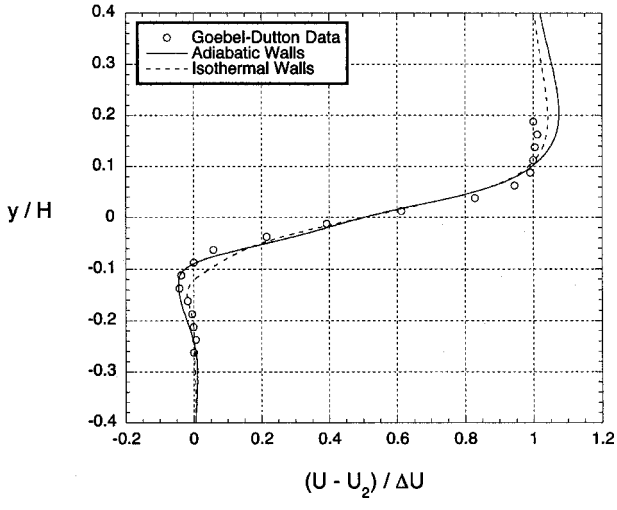

c) $X = 150$ mm

Fig. 12 Time-averaged axial velocity profiles for the cases investigating RANS thermal boundary condition effects.

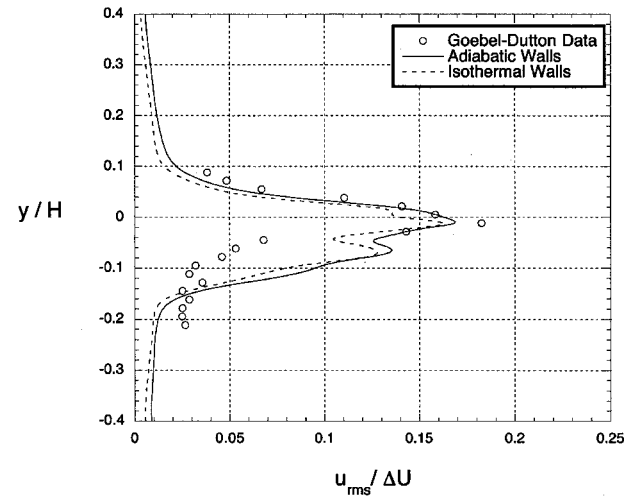

a) $X = 50$ mm

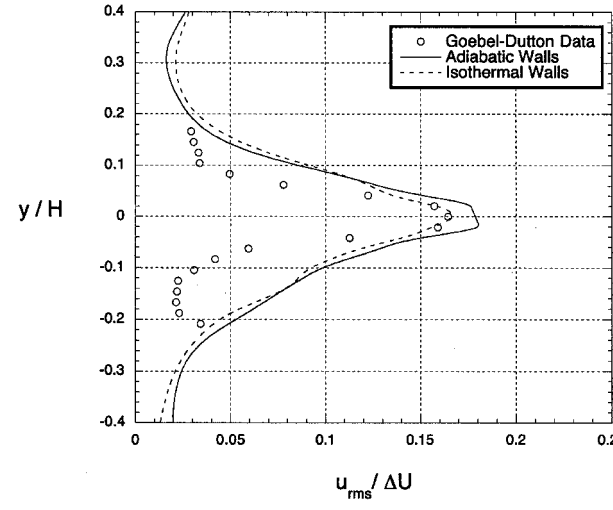

b) $X = 100$ mm

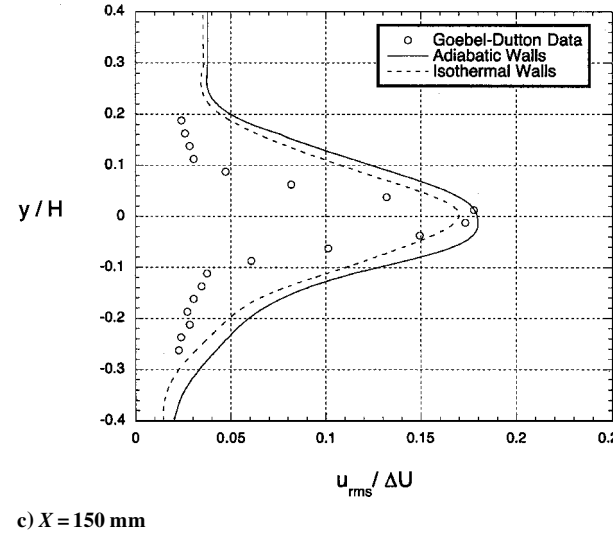

c) $X = 150$ mm

Fig. 13 Profiles of u_{rms} for the cases investigating RANS thermal boundary condition effects.

As a result, this average temperature, 419 K, was specified as the wall temperature for both streams in the new hybrid RANS/LES calculation. This case was run using the grid having a 4-mm spanwise width as a compromise between the 2-mm width grid, which was insufficient to capture three-dimensional effects, and the most computationally expensive 6-mm width grid. The results of this calculation are compared to the case from the preceding section having a 4-mm spanwise width and adiabatic walls in the RANS region.

Figure 12 shows a comparison of the mean axial velocities, demonstrating effects of the upstream RANS wall boundary conditions. The axial and vertical turbulence intensities are shown in Figs. 13 and 14, respectively. Although the mean axial velocities do not demonstrate large differences between the solutions, especially in the high shear mixing region, the comparisons of turbulence intensities generally indicate lower turbulence levels for the case in which the wall thermal boundary conditions were set to the fixed

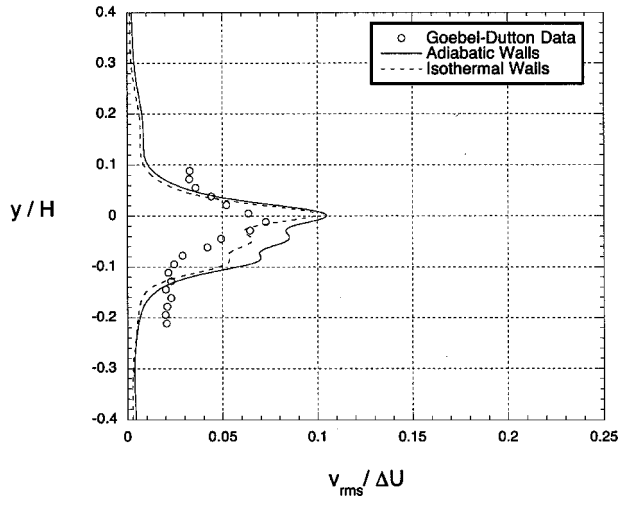

a) $X = 50$ mm

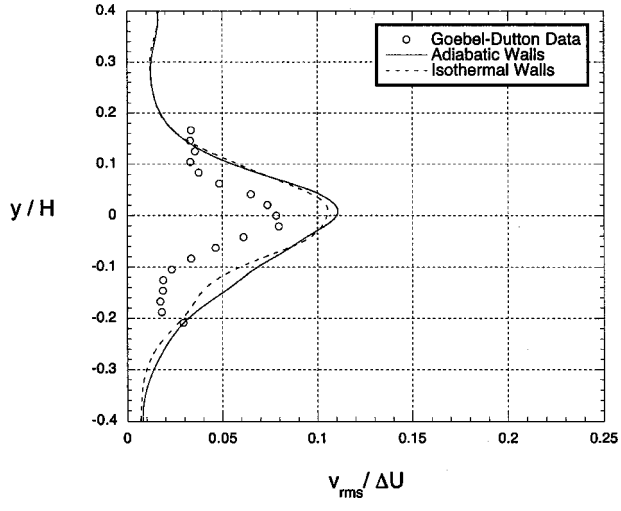

b) $X = 100$ mm

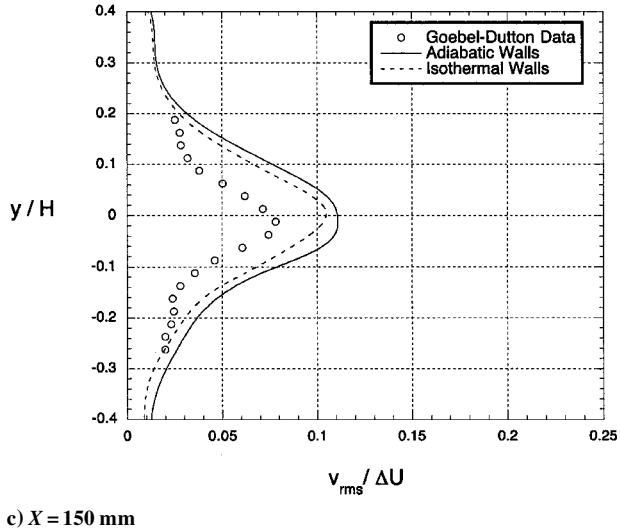

c) $X = 150$ mm

Fig. 14 Profiles of v_{rms} for the cases investigating RANS thermal boundary condition effects.

temperature, 419 K. The reduced turbulence levels in the isothermal case are in overall closer agreement with the experimental data than the adiabatic wall case.

The reason for the reduced turbulence production is as follows. With the two isolated streams matched in static pressure at the trailing edge of the splitter plate, the large difference in wall temperatures for the adiabatic walls case results in very high vertical gradients of the temperature and density profiles in the initial part of the mixing layer. With the wall surfaces instead prescribed at a fixed temperature for the other case, which is likely to be much closer to the actual situation of the experiment with the thin splitter plate, the large initial gradients in temperature and density do not occur, and the turbulent production downstream in the mixing layer is reduced.

Although the prescribed temperature specified for the two splitter plate surfaces does not result in a perfect representation of the experimental situation, such a boundary condition is very likely more appropriate than applying adiabatic walls for the mixing layer under investigation. Mixing layers in aerospace applications frequently experience similar flow conditions to those of the experiment considered here, as in the example of a hot core engine stream mixing with a cool bypass stream. The results presented in this section illustrate the importance of determining the likely thermal state of the surfaces over which boundary layers develop, especially considering likely deviations from the most frequently employed, but often improper, adiabatic wall boundary conditions.

Conclusions

The capability of a hybrid RANS/LES method to simulate a turbulent mixing layer formed from two supersonic streams was investigated. Although the RANS approach does not provide any unsteady turbulent information to the LES region, the mean flow boundary-layer characteristics are provided. The hybrid method was developed for the analysis of nozzle and mixing layer configurations in which a structural feature, such as the base region of a nozzle or splitter plate separating the upstream flows, will provide the dominant unsteady mechanism to drive the development of turbulence in the mixing layer. The most significant result was that an initial periodic vortex shedding pattern, followed by a transition to a turbulent mixing layer, was enabled by three-dimensional calculations, despite the small extent of the third dimension in these calculations. In contrast, a two-dimensional approach, by definition, does not allow such three-dimensional disturbances to develop, and it was demonstrated that a two-dimensional calculation could not predict this transition behavior. Beyond the demonstration of the hybrid method's ability to capture the qualitative behavior of the turbulent mixing layer evolution, parametric studies investigating effects of LES subgrid modeling, spanwise grid structure, and thermal boundary conditions used for the walls in the RANS region were also conducted.

In the SGS model investigations, variations in the Smagorinsky constant and the subgrid length scale were considered. The case with SGS settings producing the largest eddy viscosities resulted in the lowest turbulence levels. However, the differences among solutions was small compared to the overall discrepancy with data, indicating that other modeling issues may be more important for this specific class of flow problems. It is possible that the small spanwise domain employed here limits the generality of this conclusion, but authors such as Spalart[3] and Fureby and Grinstein[26] offer the opinion that SGS refinement will offer only small improvements for LES of flows away from boundaries and without chemical reactions. These authors further suggest that it may even be feasible to perform an LES simulation without an explicit SGS model, provided that the numerical scheme is sufficient to prevent unresolved wave numbers from contaminating the solution and that the simulation resolves turbulent scales in the inertial subrange.

The spanwise grid studies indicated that the physical width of the spanwise domain has considerable influence on the turbulent growth in the mixing layer. Although the mean flow development of the mixing layer may be considered two dimensional, the development of turbulent structures is three dimensional in nature. Widening the spanwise domain while maintaining the same resolution enabled more of the turbulent energy production to be released in the spanwise direction. This, in turn, reduced the overpredictions in the axial and vertical turbulence intensities relative to the baseline computational grid that represented the smallest width. The compromise of using only a small spanwise domain in the results reported here was necessary because of the very large number of points in the other two directions required to simulate the vortex street and transition to turbulence. However, further widening of the spanwise direction, with a proportional increase in the number of spanwise grid points, is necessary to capture more of the realistic three-dimensional mixing

layer behavior and would likely result in further improvements of the agreement between the calculations and the experiment. Continued improvements in computing speed and computer memory will hopefully make such more computationally expensive calculations routinely possible in the future.

Finally, in the investigations of the wall thermal boundary conditions used in the RANS region, an alternative to the typically used adiabatic wall boundary condition was employed, and it improved the agreement of the calculated and experimentally measured turbulence intensities. A simplified heat transfer analysis showed that the two surfaces of the splitter plate were likely much closer in temperature than that resulting from the adiabatic wall assumption. A calculation of the mixing layer was performed using an average of the surface temperatures calculated with the heat transfer analysis as the wall temperature for both RANS streams. As a result of this modification, the large gradients in temperature and density appearing in the initial portion of the mixing layer for the adiabatic walls case were substantially reduced for the modified case, which in turn resulted in lower turbulence intensities downstream in the mixing layer. These results illustrate the importance of carefully considering the thermal boundary conditions used for wall bounded regions. The capability of the hybrid method to provide not only mean flow momentum boundary-layer effects, but also the thermal boundary-layer effects, was also demonstrated by these results.

References

[1]Barber, T. J., Chiappetta, L. M., DeBonis, J. R., Georgiadis, N. J., and Yoder, D. A., "Assessment of Parameters Influencing the Prediction of Shear Layer Mixing," *Journal of Propulsion and Power*, Vol. 15, No. 1, 1999, pp. 45–53.

[2]Georgiadis, N. J., Yoder, D. A., and DeBonis, J. R., "A Comparison of Three Navier–Stokes Solvers for Exhaust Nozzle Flowfields," AIAA Paper 99-0748, Jan. 1999.

[3]Spalart, P. R., "Strategies for Turbulence Modeling and Simulations," *International Journal of Heat and Fluid Flow*, Vol. 21, No. 3, 2000, pp. 252–263.

[4]Bradshaw, P., "The Effect of Initial Conditions on the Development of a Free Shear Layer," *Journal of Fluid Mechanics*, Vol. 26, Sept. 1966, pp. 225–236.

[5]Browand, F. K., and Latigo, B. O., "Growth of the Two-Dimensional Mixing Layer from a Turbulent and Nonturbulent Boundary Layer," *Physics of Fluids*, Vol. 22, No. 6, 1979, pp. 1011–1019.

[6]Hussain, A. K. M. F., and Clark, A. R., "Upstream Influence on the Near Field of a Plane Turbulent Jet," *Physics of Fluids*, Vol. 20, No. 9, 1977, pp. 1416–1425.

[7]Georgiadis, N. J., Alexander, J. I. D., and Reshotko, E., "Development of a Hybrid RANS/LES Method for Compressible Mixing Layer Simulations," AIAA Paper 2001-0289, Jan. 2001.

[8]Spalart, P. R., Jou, W. H., Strelets, M., and Allmaras, S. R., "Comments on the Feasibility of LES for Wings, and on a Hybrid RANS/LES Approach," *Proceedings of the First AFOSR International Conference on DNS/LES*, Greyden Press, Columbus, OH, 1997, pp. 137–147.

[9]Spalart, P. R., "Trends in Turbulence Treatments," AIAA Paper 2000-2306, June 2000.

[10]Spalart, P. R., and Allmaras, S. R., "A One-Equation Turbulence Model for Aerodynamic Flows," *La Recherche Aerospatiale*, Vol. 1, No. 1, 1994, pp. 5–21.

[11]Constantinescu, G. S., and Squires, K. D., "LES and DES Investigations of Turbulent Flow over a Sphere," AIAA Paper 2000-0540, Jan. 2000.

[12]Strelets, M., "Detached Eddy Simulation of Massively Separated Flows," AIAA Paper 2001-0879, Jan. 2001.

[13]Batten, P., Goldberg, U., and Chaknavarthy, S., "Sub-Grid Turbulence Modeling for Unsteady Flow with Acoustic Resonance," AIAA Paper 2000-0473, Jan. 2000.

[14]Arunajatesan, N., Sinha, N., and Menon, S., "Toward Hybrid LES–RANS Computations of Cavity Flowfields," AIAA Paper 2000-0401, Jan. 2000.

[15]Arunajatesan, N., and Sinha, N., "Unified Unsteady RANS–LES Simulations of Cavity Flowfields," AIAA Paper 2001-0516, Jan. 2001.

[16]Gottlieb, D., and Turkel, E., "Dissipative Two-Four Methods for Time-Dependent Problems," *Mathematics of Computation*, Vol. 30, No. 136, 1976, pp. 703–723.

[17]Cebeci, T., "Calculation of Compressible Turbulent Boundary Layers with Heat and Mass Transfer," AIAA Paper 70-741, Jan. 1970.

[18]Cebeci, T., and Smith, A. M. O., *Analysis of Turbulent Boundary Layers*, Academic Press, New York, 1974, pp. 215–217.

[19]Ota, D. K., and Goldberg, U. C., "Law of the Wall with Consistent No-Slip Limit," AIAA Paper 97-2246, June 1997.

[20]Smagorinksy, J., "General Circulation Experiments with the Primitive Equations," *Monthly Weather Review*, Vol. 91, March 1963, pp. 99–164.

[21]Ragab, S. A., and Sheen, S.-C., "Large Eddy Simulation of Mixing Layers," *Large Eddy Simulation of Complex Engineering and Geophysical Flows*, 1st ed., Cambridge Univ. Press, Cambridge, England, U.K., 1993, pp. 255–285.

[22]Rogallo, R. S., and Moin, P., "Numerical Simulation of Turbulent Flows," *Annual Review of Fluid Mechanics*, Vol. 17, 1984, pp. 99–137.

[23]Choi, D., Barber, T. J., and Chiappetta, L. M., "Large Eddy Simulation of High-Reynolds Number Jet Flows," AIAA Paper 99-0230, Jan. 1999.

[24]Goebel, S. G., and Dutton, J. C., "Velocity Measurements of Compressible Turbulent Mixing Layers," AIAA Paper 90-0709, Jan. 1990.

[25]Goebel, S. G., and Dutton, J. C., "Experimental Study of Turbulent Compressible Mixing Layers," *AIAA Journal*, Vol. 29, No. 4, 1991, pp. 538–546.

[26]Fureby, C., and Grinstein, F. F., "Monotonically Integrated Large-Eddy Simulation of Free Shear Layer Flows," *AIAA Journal*, Vol. 37, No. 5, 1999, pp. 544–556.

[27]Georgiadis, N. J., "A Hybrid Numerical Method for Turbulent Mixing Layers," Ph.D. Dissertation, Dept. of Mechanical and Aerospace Engineering, Case Western Reserve Univ., Cleveland, OH, Jan. 2001.

[28]White, F. M., *Viscous Fluid Flow*, McGraw–Hill, New York, 1974, p. 640.

P. Givi
Associate Editor